A99-16193

AIAA 99-0291

Direct Numerical Simulation of Görtler Instability in Hypersonic Boundary Layers

Chong W. Whang and Xiaolin Zhong
University of California, Los Angeles
Los Angeles, CA

37th Aerospace Sciences Meeting & Exhibit
January 11–14, 1999 / Reno, NV

Direct Numerical Simulation of Görtler Instability in Hypersonic Boundary Layers

Chong W. Whang *and Xiaolin Zhong †
University of California, Los Angeles, California 90095

Abstract

The prediction of transition in hypersonic boundary layer flow is one of the fundamental interests in fluid mechanics. In general, boundary layer flows becomes turbulent in three steps: 1) receptivity, 2) linear growth of disturbance, and 3) nonlinear effects in which the flow breaks down to turbulence. When forcing disturbances are introduced into the boundary layer edge, the flow is excited and becomes turbulent due to the growth of the disturbances. Görtler vortices appear in boundary layer flow along concave surfaces and affect the flow stability conditions. It is not possible to avoid concave surfaces in engineering designs such as engine inlet. Therefore, Görtler instability becomes an important topic in fluid dynamics.

In this paper, Görtler instability is investigated using two approaches: Linear Stability Theory(LST) and Direct Numerical Simulation(DNS). Linear stability code with curvature effects is developed, and results are compared with available published papers. DNS is used to simulate Görtler vortices in hypersonic boundary layers. Two dimensional steady mean flow is computed using a fifth order explicit upwind scheme. Initial forcing disturbances are obtained from the LST code, and receptivity is applied in DNS. Linear growth of disturbances is compared with the LST code to verify the DNS.

1 Introduction

Counter rotating vortices whose rotating axis is in the streamwise direction appear in boundary layer flow along the concave surface due to the imbalance between pressure force and centrifugal force. These kind vortices are called Görtler vortices, and they play a main role in stability problem along the concave wall. In hypersonic boundary layer, flow becomes complicated because real gas effects and heating condition near the stagnation point cannot be ignored. In addition, when the hypersonic flow along the blunt body is concerned, bow shock appears in front of the body. If the blunt body contains concave surface, Görtler vortices affect the stability conditions of the flow.

Görtler vortices have been studied experimentally and numerically since Görtler found them in 1940 [1-36]. Liepmann [2] conducted boundary-layer transition experiments on concave walls and showed that the critical Re for concave walls is lower than for flat plates. In other words, concavity destabilizes the flow. Even though the Görtler instability has been theoretically estabilished since 1940, actual observation of Görtler vortices were conducted by Tani [3] in 1962. Using smoke, he observed a spanwise variations by velocity measurements along the concave wall. Aihara [4] in his wind tunnel experiment showed that the non-linear development of Görtler vortices mainly affects the transition of the boundary layer. Sabzvary and Crane [5] and Peerhossaini and Wesfreid [6] observed mushroom like vortices due to nonlinear growth. They showed there are two regions(upwash and downwash) in development of Görtler vortices pair. Peerhossaini and Wesfreid [6] also observed interaction between two neighboring vortices.

Recent experiments have shown that breakdown of Görtler vortices is mainly due to secondary instabilities. Aihara and Koyama [7] and Aihara et al [8] identified the breakdown of the vortex structure as a secondary instability due to a horsesho-vortex structure. Swearingen and Blackwelder [9] verified two kinds of secondary instabilities which are the sinous and varicose(horsesho) types. They showed that sinuous mode is produced by spanwise velocity gradient and the varicose is due to normal velocity gradient. In their experiments, the unsteady secondary instability fluctuations correlated better with the spanwise velocity than with the normal velocity gradient.

Görtler [1] in his linear stability analysis assumed parallel flow. Kahawita and Meroney [10] calculated Görtler instability problem in which normal velocity was included. In their analysis, the value of the Görtler number approaches a critical value of zero as the wavenumber reaches a limiting value of 0.3. It was a quite different results to Görtler's in which nonzero

*Graduate Student, chong@seas.ucla.edu
†Associate Professor, Mechanical and Aerospace Engineering Department, Member AIAA

critical Görtler number exists at zero wave number. Herbert [11] and Floryan [12] studied higher mode of Görtler instability, and they concluded that the growth process for the second mode is considerably slower than for the first mode.

Görtler [1], Hämmerin [13] and Smith [14] showed neutral stability curves in their linear stability analysis. However, their results were not consistent to each other. They were only matched in the limit of the short wavelength, and Hall [15] [16] [17] applied asymptotic theory to Görtler instability problems. Hall [15] proved that in high wavenumber limit, the parallel flow theory becomes valid. Hall [17] obtained that the existence of a neutral point strongly depends on location and shape of the initial condition.

Recently many researchers have tried to solve nonlinear Görtler problems numerically. Sabry and Liu [18] and Hall [19] demonstrated that nonlinear evolution of streamwise Görtler vortices produces inflextional profiles which will presumably break down. Lee and Liu [20] and Liu [21] numerically showed mushroom like vortex due to nonlinear growth of Görtler vortices.

Liu and Domaradzki [22], Yu and Liu [23], and Li and Malik [24] studied secondary instability effects on Görtler vortices. Secondary instability is produced by interaction between TS waves and Görtler vortices. Li and Domaradzki [22] dealt with Görtler problem using DNS. Initial disturbances were obtained from LST since initial stage of growing Görtler vortices is linear. They showed that Görtler vortices become turbulent due to the spanwise velocity gradient as well as the normal velocity gradient. These velocity profiles contain inflectional points which play roles in flow instability. They mentioned that varicose mode is related to the normal velocity gradient and sinuous mode is to the spanwise gradient and concluded that sinuous mode is dominant. Li and Malik [24] used PSE(parabolic stability equation) method, and studied nonlinear effects of Grotler vortices. In their approach, they showed there are two kinds of secondary instability modes; even and odd. The even mode is related to the varicos mode, and the odd mode is to the sinous mode.

The interactions between two neighboring vortices are concerned by Guo and Finlay [25]. They used Legendre spectral element method and studied Eckhaus instability due to spanwise perturbations. They figured out the vortices can attract or repulse each other depending on the wavelength of the disturbances.

Compressibility is considered as a stabilizing factor. This is also true for the boundary layer flow along the concave surface. Kobayashi and Kohama [26] in their linear stability analysis considered compressibility effects on Görtler vortices. Parallel flow approximations were assumed. They concluded compressibility has a stabilizing effect on Görtler vortices. With weak curvature, the vortices grow weakly in the stream direction; therefore, it is not possible to separate the weak growth of the boundary layer from the growth of the disturbance. In other words, nonparallel effects are important in Görtler instabilities. El-hady and Verma [27] computed complete stability digrams for various Mach number. Normal velocity and streamwise variations were included. They also proved compressibility is a stabilizing factor.

In normal mode analysis in linear stability analysis, method of separation variables is used. Hall [18] proved that normal mode solution is only valid in the limit of high wavenumber. Therefore, Spall and Malik [28] dealt with linear stability theory of Görtler instability using method of marching in which streamwise variations of disturbances were also considered. In mean flow calculation, pressure changes in streamwise direction were included to study adverse pressure effects. Mach number range is 0-12 so they considered hypersonic as well as supersonic boundary layers. It was found that in hypersonic limit, compressibility effects become less important, and adverse pressure is a dominant role in flow instability. Cooling and heating effects also play an important role in compressible flow stability. According to Spall and Malik [28], cooling destabilized the flow, and heating slightly stabilized flow when Görtler vortices are concerned.

Hall and Malik [29] and Dando [30] analyzed the role of compressibility within the large wavenumber limit. Dando [30] completed analysis fo two-dimensional and three dimensional boundary layers in the large Görtler number limit(inviscid flow). He use unit prandtl number and Chapman viscosity law.

Hall and Fu [31] in their asymptotic analysis showed that at hypersonic speed limit, the nonuniqueness of the neutral stability curve associated with incompressible Görtler vortices disappears. Fu and Hall [32] considered real gas effects on the linear stability of Görtler vortices and considered secondary instability in hypersonic limit. Recently receptivity becomes a critical issue for the Görtler problem. Denier et al [33] addressed exactly this issue by considering the vortex motion induced by wall roughness.

2 Disturbance Equations

The compressible linear stability equations originate from the compressible Navier-Stokes equations. The gas is assumed to be perfect Newtonian gas. The three dimensional Navier-Stokes equations in cartesian coordinates(x^*,y^*,z^*), where '*' denotes dimensional quantities, are

$$\rho^* \left[\frac{\partial \mathbf{u}^*}{\partial t^*} + \mathbf{u}^* \cdot \nabla \mathbf{u}^*\right] = -\nabla p^* + \nabla \cdot \left[\lambda^* (\nabla \cdot \mathbf{u}^*)\, \mathbf{I} + \mu^* (\nabla \mathbf{u}^* + \nabla \mathbf{u}^{*tr})\right], \quad (1)$$

$$\frac{\partial \rho^*}{\partial t^*} + \nabla \cdot (\rho^* \mathbf{u}^*) = 0\,, \quad (2)$$

$$\rho^* c_p^* \left[\frac{\partial T^*}{\partial t^*} + \mathbf{u}^* \cdot \nabla T^*\right] = \nabla \cdot (k^* \nabla T^*) + \frac{\partial p^*}{\partial t^*} + \mathbf{u}^* \cdot \nabla \mathbf{u}^* + \Phi^*\,, \quad (3)$$

$$p^* = \rho^* R^* T^*\,, \quad (4)$$

where $\mathbf{u}^*$ is the velocity vector, ρ^* is the density, p^* is the pressure, T^* is the temperature, R^* is the gas constant, c_p^* is the specific heat at constant pressure, k^* is the thermal conductivity, μ^* is the first coefficient of viscosity, and λ^* is the second coefficient of viscosity. The viscous dissipation function, Φ^*, is given as

$$\Phi^* = \lambda^* (\nabla \cdot \mathbf{u}^*)^2 + \frac{\mu^*}{2} [\nabla \mathbf{u}^* + \nabla \mathbf{u}^{*tr}]^2\,. \quad (5)$$

In the derivation of disturbance equations, we closely followed Malik's [37] formulation for cartesian coordinates. The flow variables and equations are nondimensionalized as follows: velocity by U_∞^*, density by ρ_∞^*, pressure by $\rho_\infty^* U_\infty^{*2}$, length scales by x^*, and time scale by x^*/U_∞^* where x^* denotes distance from the leading edge. Instantaneous flow variables are represented as the sum of mean value and fluctuations, i.e.

$$\begin{aligned} u &= \overline{U}(x,y,z) + \tilde{u}(x,y,z,t) \\ v &= \overline{V}(x,y,z) + \tilde{v}(x,y,z,t) \\ w &= \overline{W}(x,y,z) + \tilde{w}(x,y,z,t) \\ p &= \overline{P}(x,y,z) + \tilde{p}(x,y,z,t) \\ T &= \overline{T}(x,y,z) + \tilde{T}(x,y,z,t)\quad . \end{aligned} \quad (6)$$

Detailed linear disturbance equations can be found in Malik [37]. Two dimensional steady mean flow is assumed; therefore, $\overline{W}(x,y,z) = 0$ and $\frac{\partial}{\partial z} = 0$.

Resulting linear disturbance equations can be expressed in matrix form as

$$[A]\tilde{\mathbf{q}} + [B]\frac{\partial \tilde{\mathbf{q}}}{\partial t} + [C]\frac{\partial \tilde{\mathbf{q}}}{\partial x} + [D]\frac{\partial \tilde{\mathbf{q}}}{\partial y} + [E]\frac{\partial \tilde{\mathbf{q}}}{\partial z} + [F]\frac{\partial^2 \tilde{\mathbf{q}}}{\partial x^2} + [G]\frac{\partial^2 \tilde{\mathbf{q}}}{\partial y^2} + [H]\frac{\partial^2 \tilde{\mathbf{q}}}{\partial z^2} + [I]\frac{\partial^2 \tilde{\mathbf{q}}}{\partial x \partial y} + [J]\frac{\partial^2 \tilde{\mathbf{q}}}{\partial y \partial z} + [L]\frac{\partial^2 \tilde{\mathbf{q}}}{\partial x \partial z} = 0\,, \quad (7)$$

where

$$\tilde{\mathbf{q}} = \begin{bmatrix} \tilde{u}(x,y,z,t) \\ \tilde{v}(x,y,z,t) \\ \tilde{p}(x,y,z,t) \\ \tilde{T}(x,y,z,t) \\ \tilde{w}(x,y,z,t) \end{bmatrix}\,. \quad (8)$$

All matrix coefficients are function of mean values only.

Coordinate transformations are applied to Eq (7) to transform cartesian coordinates (x,y,z) into curve linear system (ξ,η,ζ). They are related geometrically (Figure 1):

$$\begin{aligned} d\xi &= R d\theta \\ \eta &= R - r \\ \zeta &= z \\ \tau &= t\quad , \end{aligned} \quad (9)$$

where R is a radius of curvature of the wall, $r = \sqrt{(x-x_c)^2 + (y-y_c)^2}$ and $\tan\theta = (x_c - x)/(y - y_c)$.

Velocity components depend on direction(Figure 2); therefore, it should be considered. Their relations are

$$u(x,y,z,t) = u'(\xi,\eta,\zeta,\tau)\cos\theta - v'(\xi,\eta,\zeta,\tau)\sin\theta \quad (10)$$

$$v(x,y,z,t) = u'(\xi,\eta,\zeta,\tau)\sin\theta + v'(\xi,\eta,\zeta,\tau)\cos\theta \quad (11)$$

$$w(x,y,z,t) = w'(\xi,\eta,\zeta,\tau)\,. \quad (12)$$

For variable radius curvature, R and θ is function of ξ.

An important feature of steady streamwise vortices within a shear layer is the convection of streamwise momentum in the normal and spanwise directions by weak velocity profiles. Therefore, governing equations

are rescaled as follows:

$$\begin{aligned}
\xi' &= \xi \\
\eta' &= \eta\sqrt{Re} \\
\zeta' &= \zeta\sqrt{Re} \\
u' &= \overline{U}(\xi,\eta) + \tilde{u}(\xi,\eta,\zeta,\tau) \\
v' &= (\overline{V}(\xi,\eta) + \tilde{v}(\xi,\eta,\zeta,\tau))\sqrt{Re} \\
w' &= \tilde{w}(\xi,\eta,\zeta,\tau)\sqrt{Re} \\
p' &= (\overline{P}(\xi,\eta) + \tilde{p}(\xi,\eta,\zeta,\tau))Re \quad ,
\end{aligned} \tag{13}$$

where

$$Re = \frac{U^*_\infty \rho^*_\infty x^*}{\mu^*_\infty} \, . \tag{14}$$

Transformation and rescale give new matrix form of disturbance equations:

$$\begin{aligned}
&[A']\tilde{\mathbf{q}}_1 + [B']\tfrac{\partial \tilde{\mathbf{q}}_1}{\partial \tau} + [C']\tfrac{\partial \tilde{\mathbf{q}}_1}{\partial \xi'} + [D']\tfrac{\partial \tilde{\mathbf{q}}_1}{\partial \eta'} \\
&+[E']\tfrac{\partial \tilde{\mathbf{q}}_1}{\partial \zeta'} + [F']\tfrac{\partial^2 \tilde{\mathbf{q}}_1}{\partial \xi'^2} + [G']\tfrac{\partial^2 \tilde{\mathbf{q}}_1}{\partial \eta'^2} + [H']\tfrac{\partial^2 \tilde{\mathbf{q}}_1}{\partial \zeta'^2} \\
&+[I']\tfrac{\partial^2 \tilde{\mathbf{q}}_1}{\partial \xi' \partial \eta'} + [J']\tfrac{\partial^2 \tilde{\mathbf{q}}_1}{\partial \eta' \partial \zeta'} + [L']\tfrac{\partial^2 \tilde{\mathbf{q}}_1}{\partial \xi' \partial \zeta'} = 0 \quad ,
\end{aligned} \tag{15}$$

where

$$\tilde{\mathbf{q}}_1 = \begin{bmatrix} \tilde{u}'(\xi',\eta',\zeta',\tau) \\ \tilde{v}'(\xi',\eta',\zeta',\tau) \\ \tilde{p}'(\xi',\eta',\zeta',\tau) \\ \tilde{T}'(\xi',\eta',\zeta',\tau) \\ \tilde{w}'(\xi',\eta',\zeta',\tau) \end{bmatrix} \, . \tag{16}$$

For normal mode analysis, disturbance form is

$$\tilde{\mathbf{q}_1} = \hat{\mathbf{q}}(\eta') e^{\alpha\xi' + \beta\zeta' - \omega\tau} \, , \tag{17}$$

where

$$\tilde{\mathbf{q}}_1 = \begin{bmatrix} \hat{u}(\eta') \\ \hat{v}(\eta') \\ \hat{p}(\eta') \\ \hat{T}(\eta') \\ \hat{w}(\eta') \end{bmatrix} \, . \tag{18}$$

When Eq(17) is substituted into Eq(15), linearized disturbance equations become a homogeneous system of ordinary differential equations:

$$(\mathbf{A_0}\, D^2 + \mathbf{B_0}\, D + \mathbf{C_0})\, \hat{\mathbf{q}} = 0 \, , \tag{19}$$

where

$$\begin{aligned}
\mathbf{A_0} &= [G'] \\
\mathbf{B_0} &= [D'] + i\alpha[I'] + i\beta[J'] \\
\mathbf{C_0} &= [A'] - i\omega[B'] + i\alpha[C'] + i\beta[E'] \\
&\quad -\alpha^2[F'] - \beta^2[H'] - \alpha\beta[L'] \, .
\end{aligned} \tag{20}$$

D is the derivative opperator in η' direction, i.e. $D = d/d\eta'$ and $D^2 = d^2/d\eta'^2$. The eigenvalue problems are solved using Chebyshev collocation global method [37] and fourth order finite different method. Boundary conditions are subjected to

$$\hat{u} = \hat{v} = \hat{w} = \hat{T} = 0 \quad at\ \eta = 0 \tag{21}$$

$$\hat{u}, \hat{v}, \hat{w}, \hat{T} \to 0 \quad as\ \eta \to \infty \, . \tag{22}$$

Our disturbance equations do not expressed Görtler number and curvature explicitly. However, they are included implicitly in transformation procedure. Therefore, to study Görtler problem, we should calculate Görtler numeber from Re, radius of curvature(R) and other flow properties (i.e. pressure and temperature). Formula of Görtler number is

$$G = Re_\delta \sqrt{\frac{\delta}{R}} \, , \tag{23}$$

where

$$\delta = \sqrt{\frac{\nu^*_\infty x^*}{U^*_\infty}} \, . \tag{24}$$

3 Results

3.1 Incompressible linear stability analysis of Görtler vortices

To deal with Görtler instability, curvature effects are included in LST code using coordinate transformations, and results are compared with previous works. Both temporal and spatial linear stability analysis are considered. Mean flows are computed from Blasius equation using shooting method. Flow variables and equations are nondimensionalized as follows: streamwise velocities by U^*_∞, normal and spanwise velocities by $U^*_\infty/\sqrt{Re}$, pressure by $\rho^*_\infty U^{*2}_\infty/Re$, length scales

by x^* in streamwise direction and by boundary layer thickness,δ^*, in normal and spanwise directions, and time scale by x^*/U^*_∞. These scalings follow from the work of Davey, Diproma and Stuart [38] on Taylor vortices, and have also been used in subsequent investigations of Görtler vortex instability.

Herbert [11] studied temporal Görtler instability and found higher mode as well as the primary in which wavenumber, α, is zero, and spanwise disturbances are introduced in the mean flow. Parallel flow approximations were assumed. In the limit of $Re \to \infty$ and large radius of curvature, governing equations of Görtler vortices in curve linear system become flat plate boundary layer equation; therefore, most people assumed the flat plate mean flow. The flow conditions are

$$\begin{aligned} G &= 6.55 \\ \beta &= 0.3824 \\ U^*_\infty &= 5m/sec \\ T^*_\infty &= 313.6K \\ R^* &= 3.2m \\ x^* &= 0.4m \quad , \end{aligned} \tag{25}$$

which Herbert used in his analysis. Görtler number, G, is defined as $Re_\delta \sqrt{\frac{\delta}{R}}$. From these conditions, we calculated Re and Mach number which are main parameters in our code. The growth rate of the primary mode is $\omega_i = 1.67$ which is very closed to the value in Herbert [11] which is 1.66. The computed value of the second mode is 0.027, and it also agrees well with the Herbert [11]'s which is 0.0. Real part of the frequency is zero for both modes. Both modes are unstable since their eigenvalues are positive. Eigenfunctions of both modes are shown in figure 3 and figure 4. Two peaks in figure 4 represent that there are two vorticity layers which are stacked together. It is more clearly represented in figure 5 which is streamwise velocity contour. Mode II contains one more layer than Mode I. Dashed lines represent negative. However, higher modes are rarely observed in experiments because growing process of these modes are much slower than one of the primary. The shapes of eigenfunctions are similar to those in Herbert [11].

Experiments show that, at the onset, Görtler vortices are generally steady. Therefore, recent papers only considered the spatial linear stability analysis in which ω is zero and β is real. To deal with spatial stability problem, α^2 terms in the disturbance equations are ignored since with these terms, we cannot solve the eigenvalue problems. These terms are usually small compared to others. The results from spatial analysis are compared Kahawita et al [10]. Normal velocity is included in the analysis, but streamwise variations are still neglected. Mean flow was assumed *Blasius boundary layer flow.*

Figure 6 show eigenfunction distributions computed using following conditions which Kahawita et al used in their analysis:

$$\begin{aligned} G &= 2.569 \\ \beta &= 1.0 \\ U^*_\infty &= 5.0m/sec \\ T^*_\infty &= 292.4K \\ P^*_\infty &= 1atm \\ R^* &= 3.2m \quad , \end{aligned} \tag{26}$$

Results by Kahawita et al [10] are also shown in the same plot. The shape of eigenfunctions are the same, but our results are shifted upward more than those in Kahawita et al. The reasons may be due to the method differences. Kahawita considered normal velocity and higher curvature terms. He expanded the curvature terms (i.e. terms associated to $(1-\kappa\eta)^{-1}$, where κ is curvature) and kept zeroth and first order terms. However, we did not use Taylor expansions for the curvature. We deal with them as mean values, so those terms are included in the matrix which are functions of mean quantities only. Also they solved eigenvalue problem locally so α^2 terms are not ignored.

3.2 Compressible linear stability analysis of Görtler vortices

Main purpose of this project is to study phenomena of Görtler instability at hypersonic limit, so flow condition is compressible. Spatial linear stability is considered since the steady Görtler vortices are generally observed in experiments. El-hady and Verma [27] computed complete stability diagrams for various Mach numbers. Therefore, our code is first verified by comparing results with El-hady et al. In this analysis, all streamwise variations are included; so growing boundary layers are concerned. Pressure is still assumed constant. Compressible mean flow of the boundary layer along the flat plate is computed using Mangler-Levy-Lees transformation and shooting methods. Flow conditions for different Mach numbers are shown in Table 1. All sets of conditions gave the same growth rate in which wavenumber (β) is 0.3 and stagnation temperature (T^*_0) is $310K$. The computed growth rates of primary modes using 100 grid points for five different Mach numbers are represented in Table 2 and compared with El-hady's results. They are well matched.

Figure 7 shows distributions of eigenfunctions of streamwise velocity, normal velocity, spanwise velocity,

Table 1: Flow properties for different Mach numbers in which $T_0^* = 310K$ and $\beta = 0.3$. El-Hady et al (1983) show five different Görtler numbers which gives the same growth rates in different Mach numbers.

Mach	G	$P_\infty^*(N/m^2)$	$T_\infty^*(K)$	$R(m)$
1	12.9289	1.013×10^5	258.3	7.8
2	12.0844	6.753×10^4	172.2	13.6
3	11.5310	4.341×10^4	110.7	20.2
4	11.4786	2.894×10^4	73.8	26.3
5	11.7611	2.026×10^4	51.7	31.4

Table 2: Growth rates of Mode I for different Mach numbers are shown and compared with El-Hady et al (1983).

Mach	G	σ(current method)	σ(El-Hady et al)
1	12.9289	-4.95880522	-5.0
2	12.0844	-4.98951110	-5.0
3	11.5310	-4.97404248	-5.0
4	11.4786	-4.93742251	-5.0
5	11.7611	-4.84224414	-5.0

and temperature. The figures show that the location of $\hat{u}_{max}$, $\hat{v}_{max}$, $\hat{w}_{max}$, and $\hat{T}_{max}$ move away from the wall as Mach number increases. This indicates that disturbances go outside of the boundary layer as Mach number increases. In order words, flow become more stable.

3.3 Curvature effects

Theoretically convex wall stabilizes flow, and the concave destabilizes flow. We have studies these effects in three different cases:1) $\alpha \neq 0.0$ and $\beta = 0.0$ 2) $\alpha = 0.0$ and $\beta \neq 0.0$, and 3) $\alpha \neq 0.0$ and $\beta \neq 0.0$.

3.3.1 Case I ($\alpha \neq 0.0$ and $\beta = 0.0$)

Nonzero alpha represents the shear mode. Curvature effects have been investigated for incompressible and compressible flows. Temporal instablity is concerned in this analysis. Figure 8 and figure 9 represent incompressible flow curvature effects since Mach number is 10^{-6}. Figure 8 shows that concave curvature does not really affects the growth rate since temporal growth rate (ω_i) dose not change depending on radius curvature. However, the convex stabilizes the flow as curvature effects become lager. Smaller radius of curvature represents more curved wall and higher curvature effects. Figure 9 shows that as the radius decreases, the growth rates decreases, and flow becomes more stable.

Concave curvature effects for compressible flow is shown in figure 10. Mach number is 10 in this analysis. At such a high Mach number, the second shear mode is dominant. Temporal growth rates plotted in figure 10 and figure 11 are for the second shear mode. It is clear that concavity destabilizes the flow since as the radius becomes smaller, growth rate increases. The role of convex wall for compressible flow is the same as one for incompressible which is represented in figure 11.

3.3.2 Case II ($\alpha = 0.0$ and $\beta \neq 0.0$)

Görtler mode is developed when spanwise disturbances are introduced on the flow along the concave surface. In other words, β is not zero for the Görtler mode. In this case, we set α is zero to study Görtler instability only. In the case of nonzero beta, there is no unstable Görtler mode for convex surface. In other words, the convex is one of stabilizing favtor in Görtler instability.

Curvature effects have been investigated for two different Mach number (0.014(figure 12) and 4.0(figure 13)). Figure 12 is temporal stability analysis, so growth rate is ω_i, and figure 13 is for the spatial analysis. Nondimensitional growth rate α_i is normalized by x^*. Both figures show that concavity has destabilizing effects on the flow condition. It is what we expected because as radius curvature decreases, Görtler number(Eq (23)) increases when other parameters remain the same. As Görtler number increases at the same β and Mach number, growth rate increases.

3.3.3 Case III ($\alpha \neq 0.0$ and $\beta \neq 0.0$)

In this case, there may exist both shear and Görtler modes. We found a condition in which both modes exist. Wave number (k) is equal to 0.117, and we change angle(θ) to study how shear and Görtler modes affect the flow stability conditions (See vector digram in figure 16 and figure 17). When the angle is 0°, it becomes case I, and 90° represents case II.

Figure 14 and figure 15 show eigenspectrum of modes. Figfure 14 is for the flat plate ,and Figure 15 is for the curved wall. General shapes are the same, however, the right blanches of the spectrums are dif-

ferent. When there is curvature effects, flat bed region appears(figure 15). Figure 16 also represents the destabilizing effects of concavity at various angle θ.

It is interesting that in which conditions Görtler mode is dominant. As angle, θ, decreases from 90°, Görtler mode changes to shear mode (figure 17). Critical angle at $Ma = 2.5$, $R = 3000$, $k = 0.117$, and $r = 5m$ is about 89°. In this flow condition, Görtler mode is dominant since the growth rate at 90° is larger than maximum growth rate of the shear mode. Figure 17 shows that very small magnitude of α changes mode from the Görtler to the shear. This trend is well represented in change shapes of the eigenvalue spectrum (figure 18) and eigenfunctions of u_r and p_r (figure 19). Figure 18 shows that as the angle decreases, the structure become more y-shaped, and the primary mode moves to the left branch of y-shape. This trend is more clearly represented in eigenfunction of p_r (Figure 19). As the angle decreases, number of peaks of p_r becomes two from one. It shows that Görtler mode becomes the first mode, and the critical angle is 88.8°.

3.4 Simulation of Flow along the Blunt Body with Concave Surface

3.4.1 2D mean flow

The steady flow solutions of the Navier-Stokes equations for the viscous hypersonic flow over blunt body is simulated using a fifth order explicit upwind scheme and shock fitting method [39]. Eight computational zones are used which are resolved by 161 × 121 grids in each zones. Stretched grids are used in streamwise direction as well as in normal direction in order to resolve rapid changes of flow properties near the stagnation point in zone 1 and viscous layers. For other zones, streamwise stretching is not necessary; however, it is used in current analysis.

First two zones are parabolic blunt body, and concave surface is extended in the other zones. Using polynomial equations, we make continuous and smooth curves. At transition points between two polynomial equations, zeroth, first, and second order derivatives are matched; therefore, curves are continuous till second order derivatives. More smooth curves can be generated by matching the third order and more, but in our analysis, we matched till second order in order to get continuous radius curvature which is a function of first and second order derivatives. For the concave surface, we used large radius of curvature to avoid shock formation due to compressive waves inside the computational domains.

The specific flow conditions are

$$\begin{aligned} M_\infty &= 15 \\ T^*_\infty &= 101.059K \\ P^*_\infty &= 10.3Pa \\ T^*_w &= 1000K \\ Re_\infty &= 150753.175 \end{aligned} \tag{27}$$

The body surface is assumed to be a non-slip wall with an isothermal wall temperature T^*_w.

Numerical solutions of the steady mean flow are represented in figure 20. Temperature and pressure are nondimensionalized by the flow variables beyond the shock. The numerical solution for the dimensionless bow shock normal velocities are in order of 10^{-8} - 10^{-9}. Both figures show the evidence of concavity. Concave wall starts when x is approximately 0.5, and the figures show that flow properties change after that point. Temperature distribution across the boundary layer in two different regions (convex and concave) is shown in figure 21. Y_n represents the normal distance from the wall. In convex wall region, maximum temperature decreases as flow moves along the surface; however opposite trends are observed in concave region. Pressure distributions are shown in figure 22. Increase pressure in the region of the concave surface mainly affects Görtler stability condition of the flow at hypersonic speed [28]. Favorable pressure gradients are shown in convex region (figure 22 (up)) and adverse pressures in concaved region (figure 22 (bottom)).

3.4.2 Initial disturbances and spatially growing Görtler vortices

Concave surfaces are included in zone 4-7. Calculated Görtler number is between 2.5-9.0, and Mach number behind shock is 6-8.5. Since Görtler number is relatively low at such high Mach number, zone 4 and 5 do not have unstable modes in LST calculation. At the end of zone 6, we found unstable Görtler mode, therefore, we gave the initial disturbances in inlet of zone 7 (figure 25). Eigenfunctions of the primary and second Görtler modes obtained from linear stability analysis using the simulated mean flow are shown in figure 23 and figure 24 respectively. The growth rate of primary mode is larger than one of the second mode. It means that primary mode is a dominant mode.

Inlet boundary conditions are

$$\begin{aligned} u &= \overline{U}(x,y,z) + \epsilon\hat{u}_r(x,y,z,t)\cos(\beta z) \\ v &= \overline{V}(x,y,z) + \epsilon\hat{v}_r(x,y,z,t)\cos(\beta z) \\ w &= \overline{W}(x,y,z) - \epsilon\hat{w}_i(x,y,z,t)\sin(\beta z) \\ p &= \overline{P}(x,y,z) + \epsilon\hat{p}_r(x,y,z,t)\cos(\beta z) \\ T &= \overline{T}(x,y,z) + \epsilon\hat{T}_r(x,y,z,t)\cos(\beta z) \quad , \end{aligned} \tag{28}$$

where $\hat{u}_r$, $\hat{v}_r$, $\hat{w}_i$, $\hat{p}_r$, anf $\hat{T}_r$ are eigenfunctions obtained from LST. Other eigenfunctions ($\hat{u}_i$, $\hat{v}_i$, $\hat{w}_r$, $\hat{p}_i$, anf $\hat{T}_i$) are zero. Since steady Görtler vortices are observed in experiments, we start to study spatial Görtler instability. In spatial linear stability analysis, ω is zero; therefore, eigenfunctions do not depend on time, and initial disturbances at inlet of zone 7 are fixed as time changes. Initial disturbances propagates spatially and converged to steady state condition.

We used four points in z-direction to cover one wavelength of spanwise disturbances. Spectral method is applied to spanwize direction to get accurate results. Wavelength is calculated from wavenumber β. In the current computation, nondimensional β is 0.1 whcih is normalized by boundary layer thickness δ and gives maximum growth rate.

To verify the DNS code, simulated results are compared with LST. We set ϵ is 0.001 which makes disturbances grow linearly, and results can be compared with LST. Figure 26 shows the temperature perturbation contours of primary(up) and second(bottom) modes in the simulation. The growth of the Görtler vortices in the streamwise direction is shown by the intensity of the disturbances.

Figure 27 shows the streamwise velocity contours of the primary(up) and the second(bottom) modes at later station (I=100). One more vorticity layer appears in second mode. Prediction by LST is also ploted in the same figure. The simulated results are matched with ones from LST. We used four points in spanwise direction, therefore, sharp points appears in contours. If we use more points, it will be resolved.

Figure 28 and figure 29 show distributions of simulated disturbances in normal direction at $I = 100$. LST results are also plotted in the same figures. u_r and T_r from DNS are matched well with those from LST. v_r and w_i show that shapes are the same, but their amplitudes are little different. The reason is because order of magnitudes of u_r and T_r is one order higher than those for v_r and w_i. When the values are compared, they are different in 10^{-5} digit. Because of higher order of magnitude, u_r and T_r seem to be more accurate.

Distributions of velocity (u_r) and temperature (T_r) along the streamwise direction are shown in figure 30. There are three curves in each figures which represent four points in z direction. The figures indicate the growing disturbances since their amplitude increases as flow moves. The results predicted by LST are also plotted in the same figures and matched well with the simulated results.

3.4.3 Blowing and suction

Engine inlet contains concave surface, and air and fuel is mixed near inlet. Fuel injection will be applied to the compression surface entrance of the inlet to study mixing effects on the Görtler instability (figure 31). First we tried to verify our code. Using computed mean flow at zone6, we give blowing and suction at inlet of zone6 which diturbes flow, but net amount of incoming flow is zero. We changed boundary condition of normal velocity at the surface of inlet as

$$v^* = \sin(\beta^* z) \, , \tag{29}$$

where nondimentional β is 0.1, and length of z is one wavelength. This condition gives spanwise disturbances.

Figure 32 shows that two kinds of disturbances develops. Görtler instability appears near the surface. Other kinds of mode appears top of the Görtler modes, but it seems to go away and Görtler mode becomes dominant as flow moves. It is shown in figure 33 and figure 34 in which the combined mode is shown at early station, but they are detached later station. Top mode decays as flow moves, and clear Görtler mode develops near the surface. Computational domain of zone 6 is not large enough to show that the top mode decays out. The whole domain of zone 6 is the transitional state; therefore, the results are not camparable to LST. However, the analysis shows that Görtler mode develops at the spanwise disturbed flow along the concave surface.

4 Conclusion

The main focus of this paper was to verify linear growing Görtler vortices using two methods:LST and DNS. We developed the LST code which includes curvature effects. Incompressible and compressible flow stabilities were computed using a compressible stability code, and results were compared with available published works. It was shown that the code gave good agreements with previous results. Curvature effects on shear

and Görtler instabilities have been calculated. It was clear that concavity destabilizes the flow, and convex curvature stabilizes the flow.

Mean flow along the blunt body which includes concave wall was simulated by a fifth-order explicit unsteady computer code. It showed a clear adverse pressure region due to the concave surface. The three dimensional mean flow was simulated using two dimensional data since we assume there are no spanwise changes. Disturbances computed by the stability code were added in inlet of zone 7. Simulation results were compared with results predicted by LST. There was good agreements between the two results. Finally we specified wave number (β) in inlet using blowing and suction and simulated the flow. The numerical simulation show the development of Görtler mode.

5 Future Works

Work is in progress to include bow shock effects and study nonlinear Görtler instability. To study bow shock effects on Görtler instability, boundary layer flow without shock will be investigated. Nonlinear study of Görtler instability includes interactions with other forms of disturbances(eg. TS waves, cross flow effects etc.) and mixing effects when fuel injection is applied in front of engine inlet.

Acknowledgments

This research was supported by the Air Force Office of Scientific Research under grant numbers F49620-95-1-0405 and F49620-97-1-0030 monitored by Dr. Len Sakell.

References

[1] Görtler, H., "Instabilita-umt laminarer Grenzchichten an Konkaven Wäden gegenber gewissen dreidimensionalen Störungen," *ZAMM*, Vol. 21, 1941, pp. 250–52.

[2] Liepmann, H. W., "Investigation of boundary layer transition on cancave walls," *NACA Rep.*, Vol. W-107, 1945.

[3] Tani, I., "Production of longitudinal vortices in the boundary layer along a concave wall," *J. Geophysical Res.*, Vol. 67 no 8, 1962, pp. 3075–80.

[4] Aihara, Y., "Görtler vortices in the nonlinear region," In Theoretical and Experimental Fluid Mechanics, ed U. Müller, K. G. Roesner, B. Schmidt, pp 331-38. Berlin:Springer-Verlag, 1979.

[5] Sabzvari, J. and Crane, R. I., "Effect of Görtler vortices on transitional boundary layers," *ASME FED*, Vol. 32, 1985.

[6] Peerhossaini, H. and Wesfreid, J. E., "Experimental study of the Taylor-Görtler Instability," In Propagation in Systems Far From Equilibrium, ed. J. E. Wesfreid, H.R. Brand, D. Manneville, G. Albinet, N. Boccara, et al, pp. 399-412. Berlin:Springer-Verlag, 1988.

[7] Aihara, Y. and Koyama, H., "Nonlinear development and secondary instability of Görtler Vortice," In Stability in the Mechanics on Continua, ed F. H. Schroeder, pp 345-54. Berlin: Springer-Verlag, 1982.

[8] Aihara, Y., Tomita, Y., and Ito, A., "Generation, development and distortion of longitudinal vortices in boundary layers along concave and flat plates," In Laminar-Turbulent Transition, ed V. V. Kozlov, pp. 447-54. New York:Springer-Verlag, 1985.

[9] Swearingen, J. D. and Blackwelder, R. F., "The growth and breakdown of streamwise vortices in the presence of a wall," *J. Fluid Mech.*, Vol. 182, 1987, pp. 255–290.

[10] Kahawita, R. and Meroney, R., "The influence of heating on the stability of laminar boundary layers along concave curved walls," *J. Applied Mech.*, 1977, pp. 11–17.

[11] Herbert, T., "Higher eigenstates of Görtler vortices," In Theoretical and Experimental Fluid Mechanics, ed U. Müller, K. G. Roesner, B. Schmidt, pp 322-30. Berlin:Springer-Verlag, 1979.

[12] Floryan, J. M., "The second mode of the Görtler instability of boundary layer," *J. AIAA*, Vol. 23, 1985, pp. 1828–30.

[13] Hämmerin, "Uber die stabilität einer kompressiblen Stömung längs einer konkaven wand dei verschienden wandtemperaturverhältnissen." Deutsch Versuchsanstalt für Lufi fahrt, Bericht 176.

[14] Smith, A., "On the growth of Taylor-Görtler vortices along highly concave wall," *Quart. J. Math*, Vol. 13, pp. 233–262.

[15] Hall, P., "Taylor-Görtler vortices in fully developed or boundary-layer flows: linear theory," *J. Fluid Mech.*, Vol. 124, 1982, pp. 475–494.

[16] Hall, P., "On the non-linear evolution of Görtler vortices in non-parallel boundary layers," *IMA J. Appl. Math.*, Vol. 29, 1982, pp. 173–196.

[17] Hall, P., "The linear development of Görtler vortices in growing boundary layers," *J. Fluid Mech.*, Vol. 130, 1983, pp. 41–58.

[18] Sabry, A. S. and Liu, T. C., "Nonlinear development of Görtler vortices and the generations of high shear layers in the boundary layer," 1988, pp. 175–83.

[19] Hall, P., "The nonlinear development of Görtler vortices in growing boundary layers," *J. Fluid Mech.*, Vol. 193, 1988, pp. 243–66.

[20] Lee, K. and Liu, T. C., "On the growth of mushroomlike structure in nonlinear spatially developing Görtler vortex flow," *Phys. Fluids A*, Vol. 4(1), 1992, pp. 95–103.

[21] Liu, T. C., "On scalar transport in nonlinearly developing Görtler vortex flow," *Geophys. Astrophys. Fluid Dynamics*, Vol. 58, 1991, pp. 133–45.

[22] Liu, W. and Domaradzki, J. A., "Direct numerical simulation of transition to turbulence in Görtler flow," *J. Fluid Mech.*, Vol. 246, 1993, pp. 267–299.

[23] Yu, X. and Liu, T. C., "On the mechanism of sinous and varicose modes in three-dimensional viscous secondary instability of nonlinear Görtler rolls," *Phys. Fluids*, Vol. 6(2), 1994, pp. 736–50.

[24] Li, F. and Malik, M., "Fundamental and subharmonic secondary instabilities of Görtler vortices," *J. Fluid Mech.*, Vol. 297, 1995, pp. 77–100.

[25] Guo, Y. and Finlay, W. H., "Wavenumber selection and irregularity of spatially developing nonlinear Dean and Görtler vortices," *J. Fluid Mech.*, Vol. 264, 1994, pp. 1–40.

[26] Kobayashi, R. and Kohama, Y., "Taylor-Görtler instability of compressible boundary layers," *J. AIAA*, Vol. 45, No. 12, 1977, pp. 1723–7.

[27] El-Hady, N. M. and Verma, A. K., "Growth of Görtler vortices in compressible boundary layers along curved surfaces," *J. Engineering and Appl. Sciences*, Vol. 2, 1983, pp. 213–38.

[28] Spall, R. E. and Malik, M. R., "Görtler vortices in supersonic and hypersonic boundary layers," *Phys. Fluids*, Vol. 1(11), 1989, pp. 1822–35.

[29] Hall, P. and Malik, M. R., "The growth of Görtler vortices in compressible boundary layers," *J. Engi. Math.*, Vol. 23, 1989, pp. 239–51.

[30] Dando, A. H., "The compressibe Görtler problem in two-dimensional boundary layers," *IMA J. Appl. Math.*, Vol. 51, 1993, pp. 27–67.

[31] Hall, P. and Fu, Y., "On the Görtler vortex instability mechanism at hypersonic speed," *Theoret. Comput Fluid Dynamics*, Vol. 1, 1989, pp. 125–34.

[32] Fu, Y. and Hall, P., "Effects of Görtler vortices, wall cooling and gas dissociation on the Rayleigh instability in a hypersonic boundary layer," *J. Fluid Mech.*, Vol. 247, 1993, pp. 503–25.

[33] J. P. Danier, P. H. and Seddougui, S. O., "On the receptivity problem for Görtler vortices: vortex motion induced by wall roughness," *Phil. Trans. R. Soc. Lond. A*, Vol. 335, 1991, pp. 51–85.

[34] Hall, P., "Görtler vortices in growing boundary layers: the leading edge receptivity problem, linear growth and the nonlinear breakdown stage," *Mathematika*, Vol. 37, 1990, pp. 151–189.

[35] Floryan, J. M., "On the Görtler instability of boundary layers," *Prog. Aerospace Sci.*, Vol. 28, 1991, pp. 235–271.

[36] Saric, W. S., "Görtler vortices," *Annual Review of Fluid Mechanics*, 1994, pp. 379–409.

[37] Malik, M. R., "Numerical methods for hypersonic boundary layer stability," *J. Comput. Phys.*, Vol. 86, 1990, pp. 376–413.

[38] Davey, A., Diprima, R. C., and Stuart, J. T., "On the instability of Taylor vortices," *J. Fluid Mech.*, Vol. 31, 1968, pp. 17–52.

[39] Zhong, X., "Direct numerical simulation of hypersonic boundary-layer transition over blunt leading edges, partI: a new numerical method and validation," *AIAA 97-0755*, 1997.

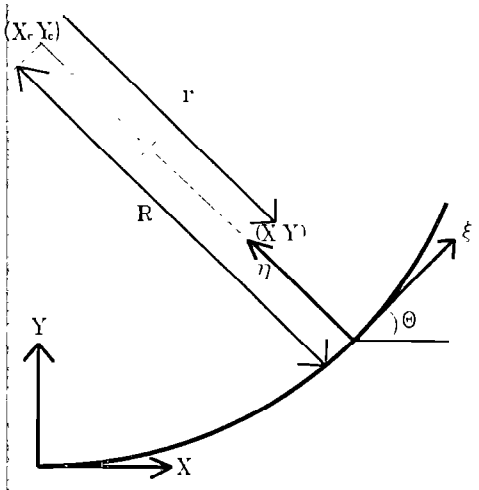

Figure 1: Schematic of coordinates.

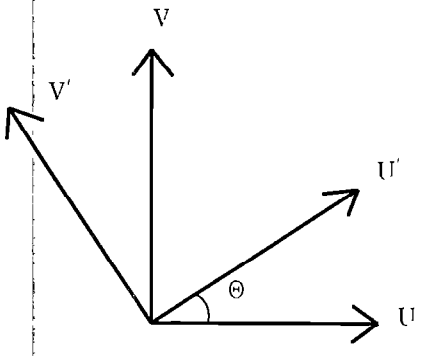

Figure 2: Schematic of velocity vector which represents the relationship of velocity components in two different coordinate systems.

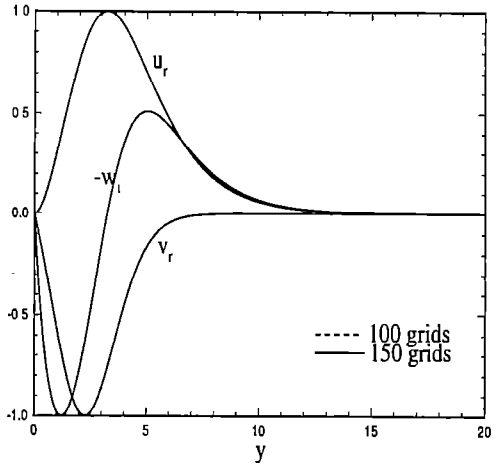

Figure 3: Velocity distributions of mode I at $G = 6.55$, $U^*_\infty = 5\text{m/sec}$, $R^* = 3.2m$, and $\beta = 0.56$.

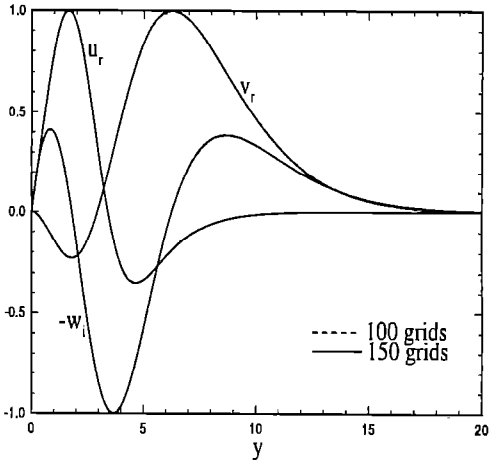

Figure 4: Velocity distributions of mode II at $G = 6.55$, $U^*_\infty = 5m/sec$, $R^* = 3.2m$, and $\beta = 0.56$.

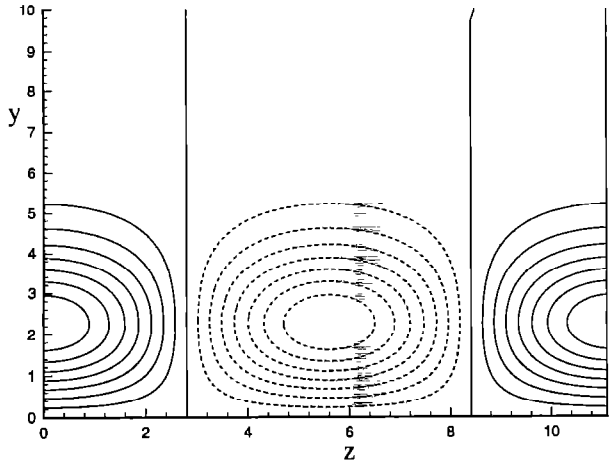

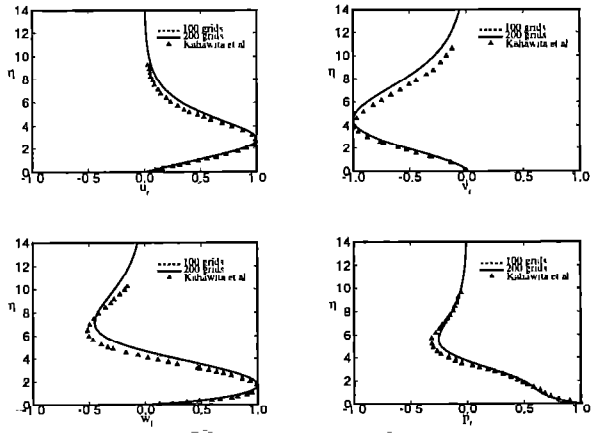

Figure 6: Eigenfunction distributions of the first mode in two different sets of grids at $G = 2.569$, $R = 3.2m$, $T^*_\infty = 292.4K$, $U^*_\infty = 5m/sec$, and $\beta = 1.0$ (Streamwise velocity, normal velocity, spanwise velocity, and pressure). Results are compared with Kahawita et al(1979).

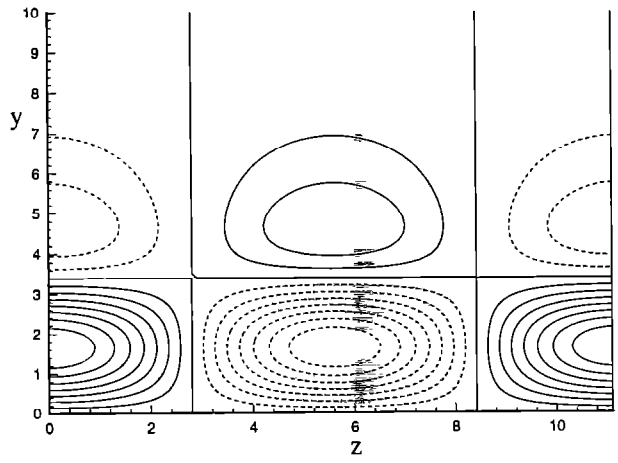

Figure 5: Streamwise velocity contour of mode I (top) and mode II (bottom) at $G = 6.55$, $U^*_\infty = 5$m/sec, $R^* = 3.2m$, and $\beta = 0.56$.

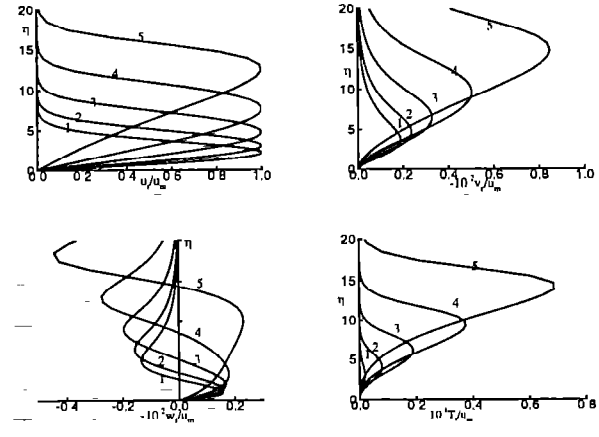

Figure 7: Streamwise(upper left), normal(upper right), and spanwise(lower left) velocity and temperature(lower right) distributions for the primary mode at $\beta = 0.3$ and $T_0 = 310K$ in which Mach number range is 1-5.

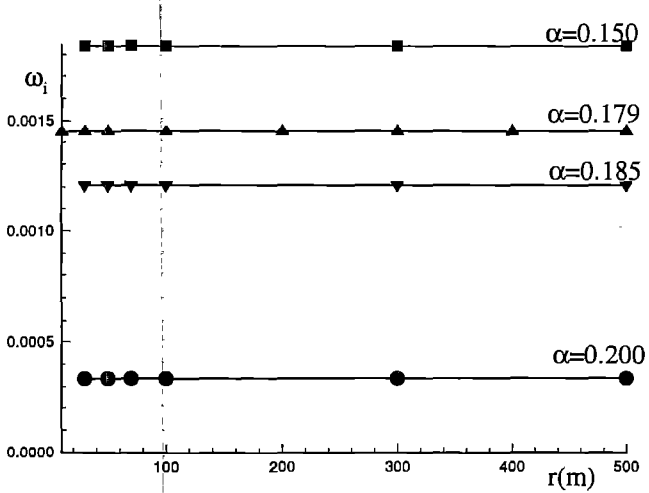

Figure 8: Concave curvature effects on dominant temporal unstable shear mode at $R = 580$ and $M = 10^{-6}$.($\alpha \neq 0.0$ and $\beta = 0.0$)

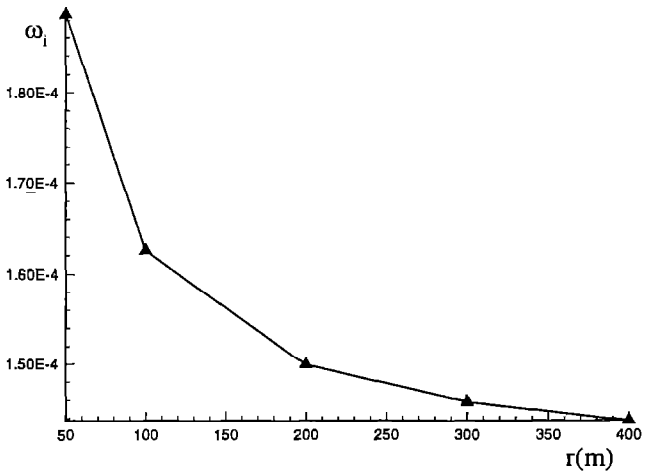

Figure 10: Concave curvature effects on dominant temporal unstable shear mode at $R = 1000$,$M = 10.0$, $\alpha = 0.12$ and $\beta = 0.0$.

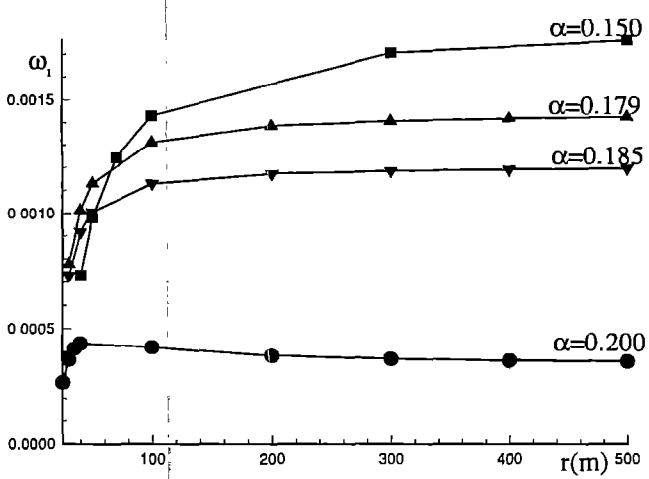

Figure 9: Convex curvature effects on dominant temporal unstable shear mode at $R = 580$ and $M = 10^{-6}$.($\alpha \neq 0.0$ and $\beta = 0.0$)

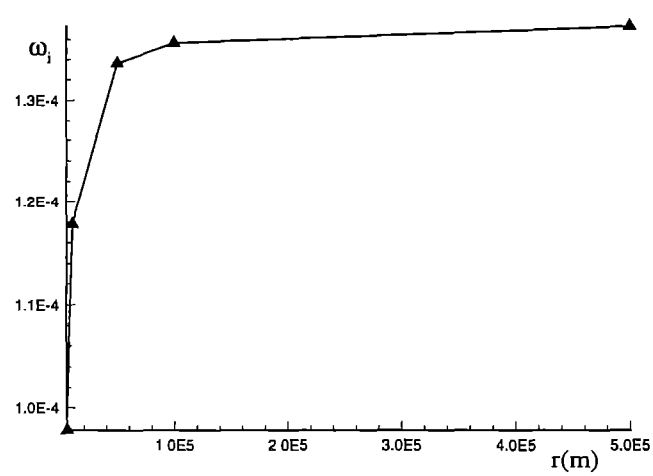

Figure 11: Convex curvature effects on dominant temporal unstable shear mode at $R = 1000$, $M = 10.0$, $\alpha = 0.12$ and $\beta = 0.0$

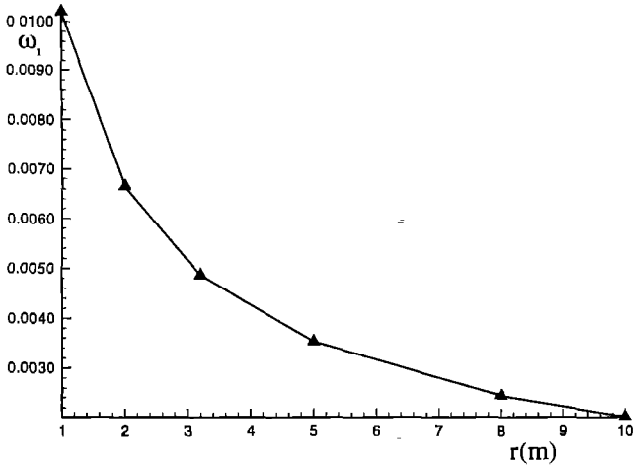

Figure 12: Concave curvature effects on dominant temporal unstable Görtler mode at $R = 343$ and $M = 0.014$,$\alpha = 0.0$ and $\beta = 0.56$

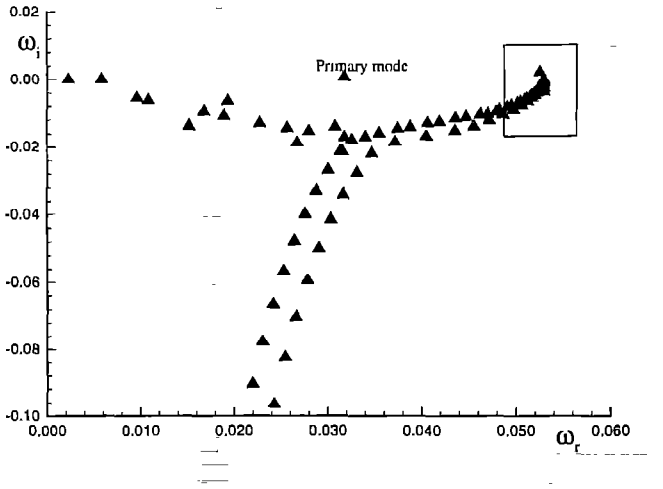

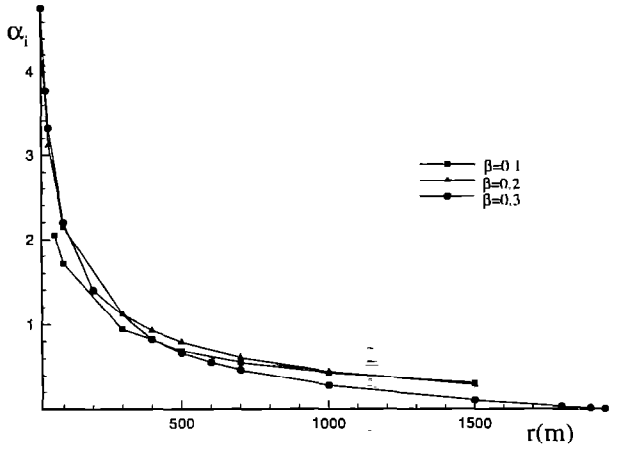

Figure 13: Concave curvature effects on dominant spatial unstable Görtler mode at $R = 8657$, $M = 4.0$ and $\alpha = 0.0$

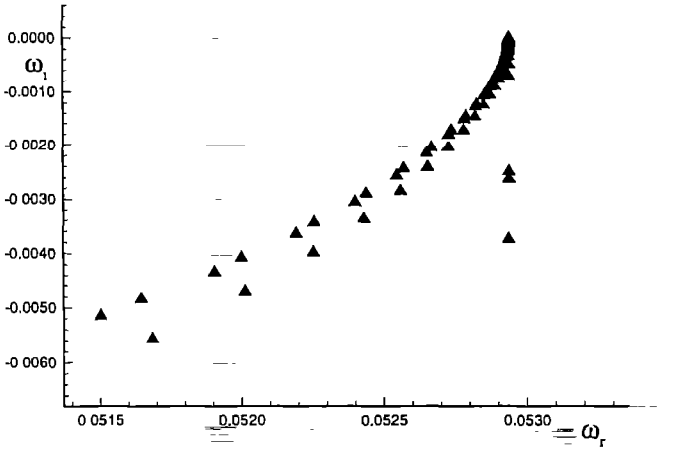

Figure 14: Eigenspectrum(left) of modes for flat plate at $R = 3000$, $M = 2.5$,$k = 0.117$, and $\theta = 63.0°$. Right figure represent the rectangular region in the spectrum.

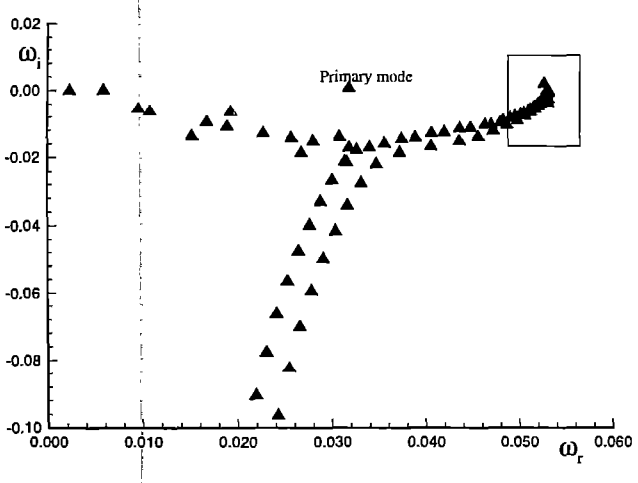

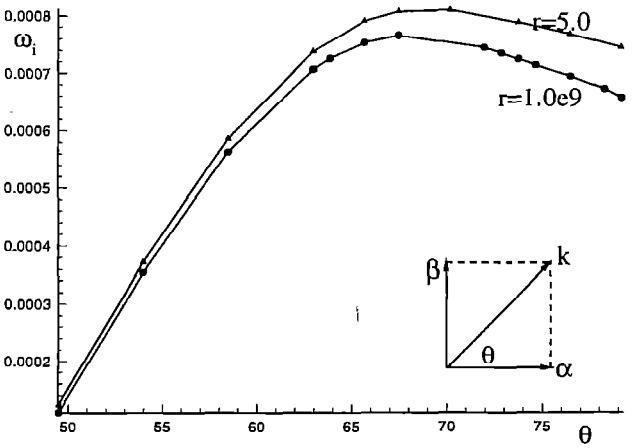

Figure 16: Magnitude of growth rate for the primary mode for flat plate and curved surface changes for various angle(θ) at $R = 3000$, $M = 2.5$ and $k = 0.117$.

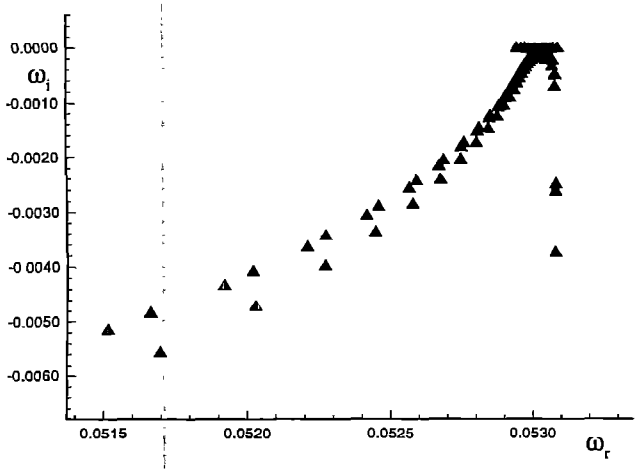

Figure 15: Eigenspectrum(left) of modes for curved surface, whose radus of curvature is 5.0, at $R = 3000$, $M = 2.5$,$k = 0.117$, and $\theta = 63.0°$. Right figure represent the rectangular region in the spectrum.

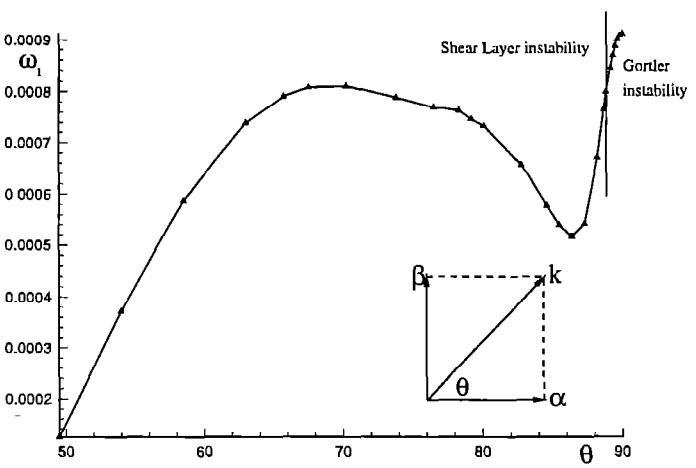

Figure 17: As θ increases, shear mode becomes Görtler modes at $R = 3000$, $M = 2.5$ and $k = 0.117$. Görtler mode is dominant since growth rate of Görtler mode is greater than one of shear mode.

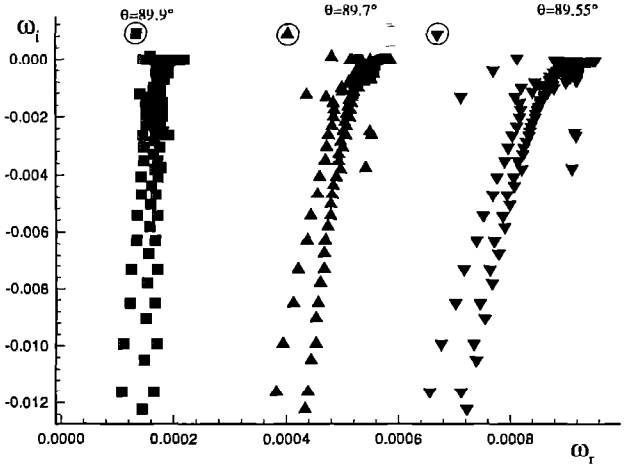

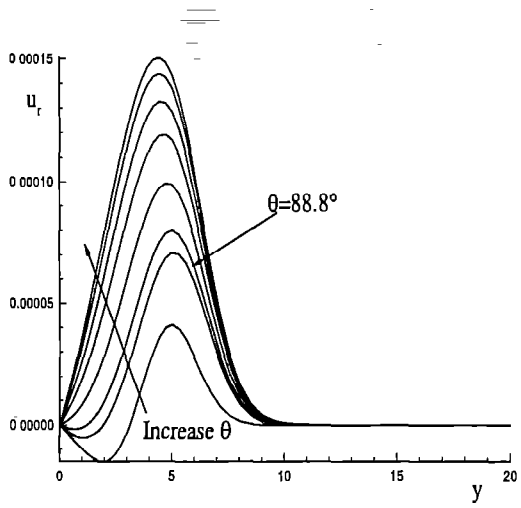

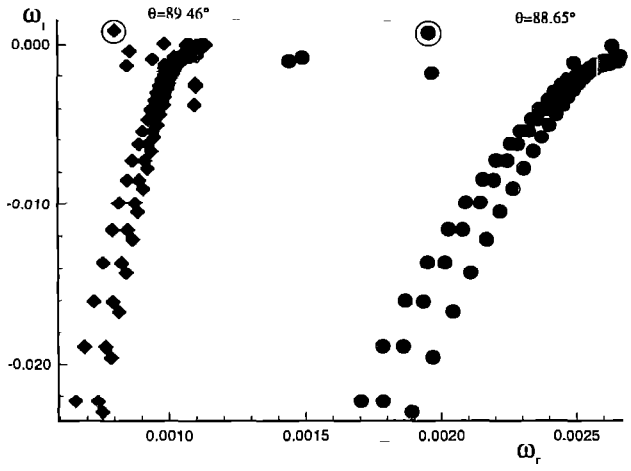

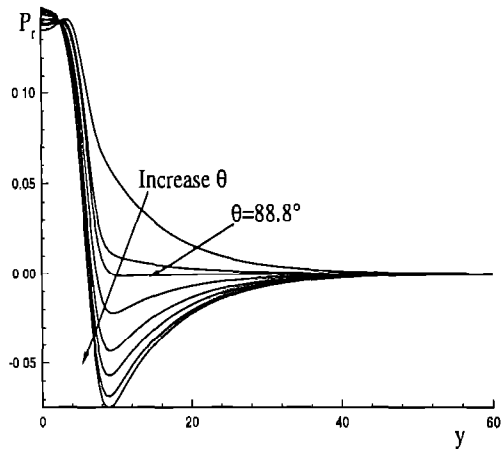

Figure 18: Structure of eigenspectrum changes as θ changes at $R = 3000$, $M = 2.5$ and $k = 0.117$. The primary mode moves to the left branch of the y-shaped eigenstructure (primary modes are circled in each spectrums). It means the mode becomes the primary shear mode as θ decreases.

Figure 19: Change shapes of eigenfunctions (u_r and p_r) indicates mode changes at $R = 3000$, $M = 2.5$ and $k = 0.117$.

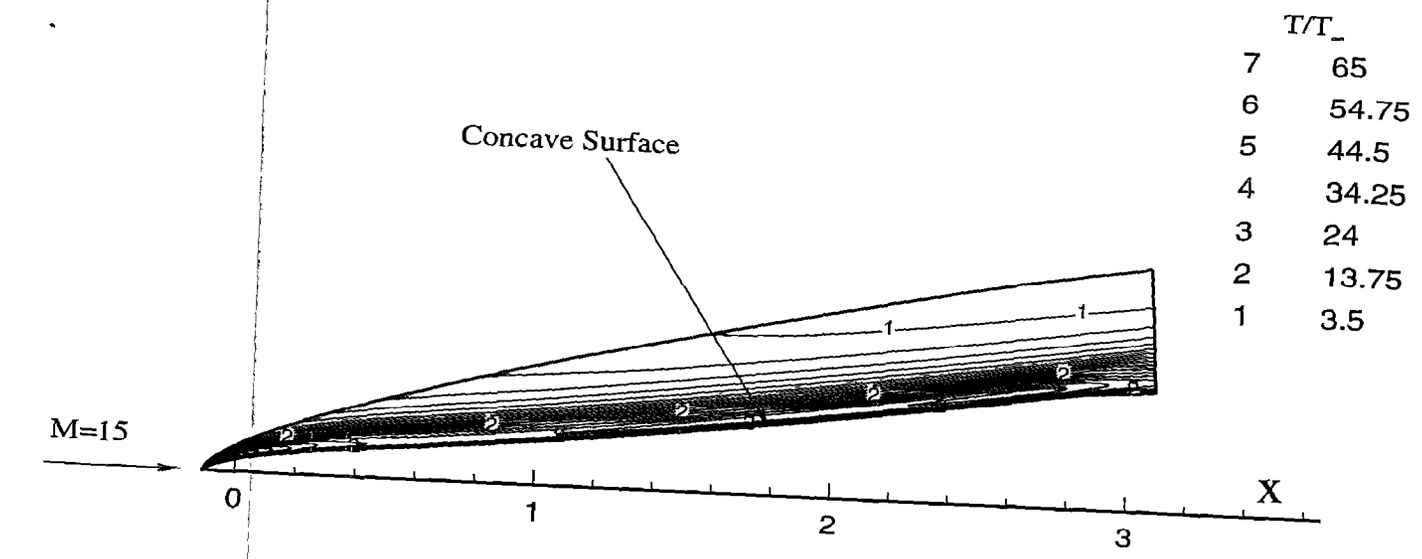

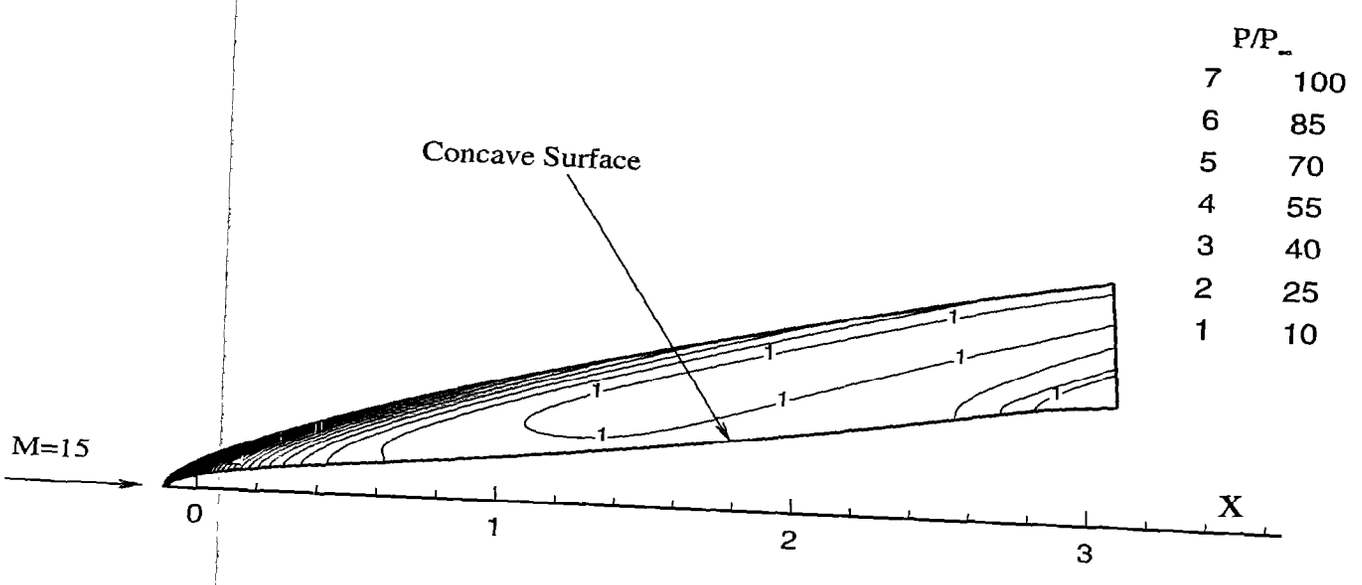

Figure 20: Temperature(upper) and pressure(bottom) contours for the steady mean flow at $M_\infty = 15$, $T^*_\infty = 101.059$ K, $P^*_\infty = 10.3$ Pa, $T^*_w = 1000$ K, $Re_\infty = 150753.17$.

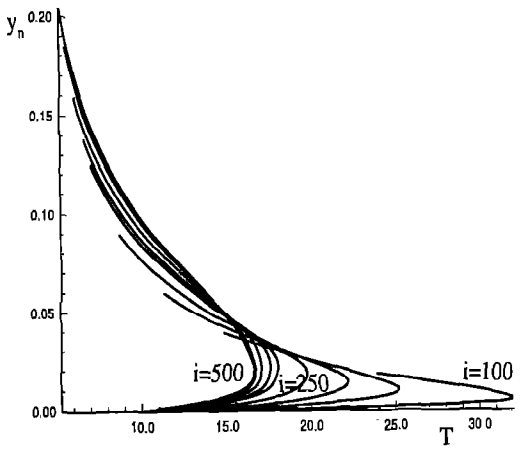

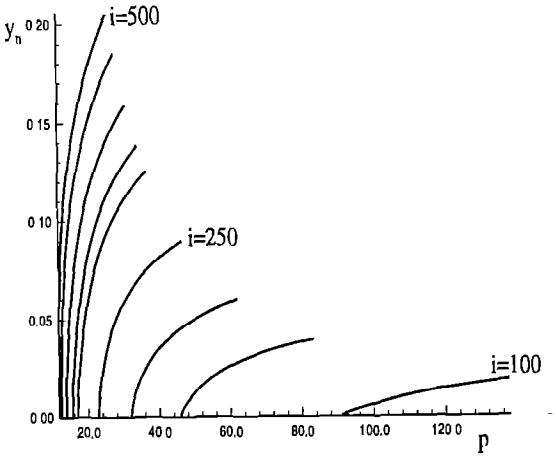

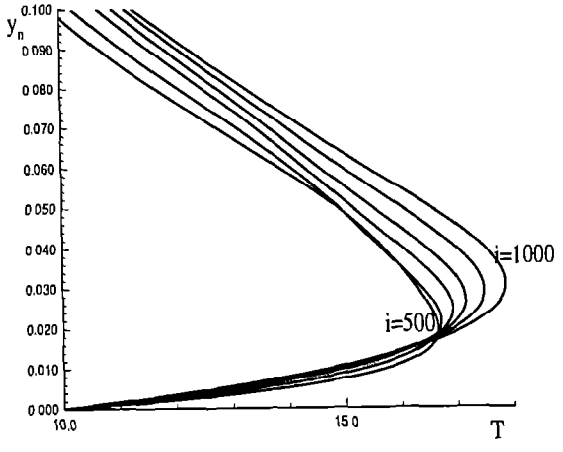

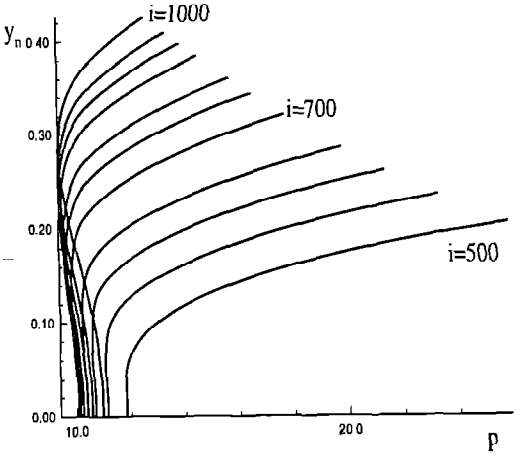

Figure 21: Variation of temperature along grid lines normal to the surface at several i grid stations: in convex region (up) and in concave region (bottom).

Figure 22: Variation of pressure along grid lines normal to the surface at several i grid stations: in convex region (up) and in concave region (bottom).

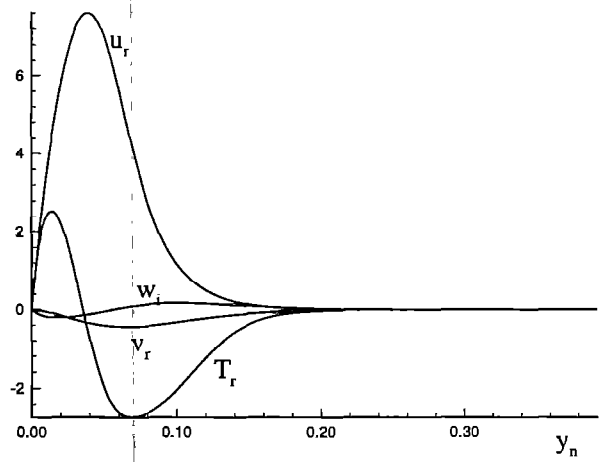

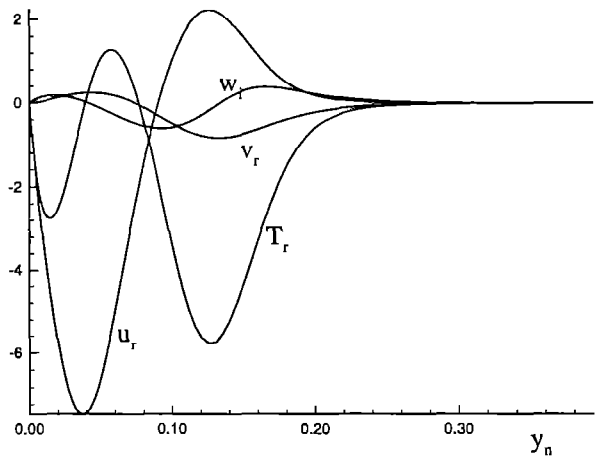

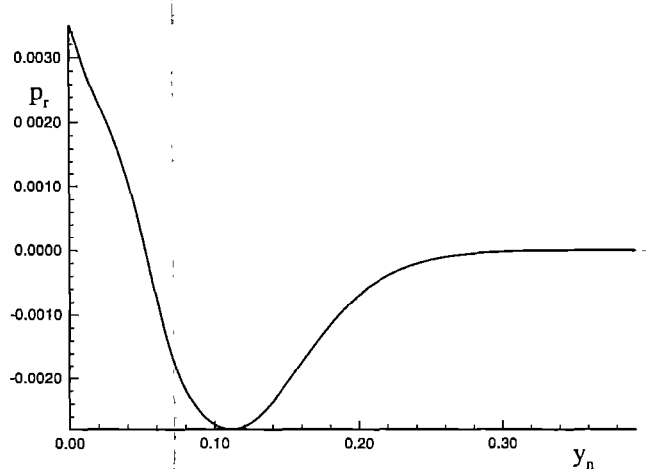

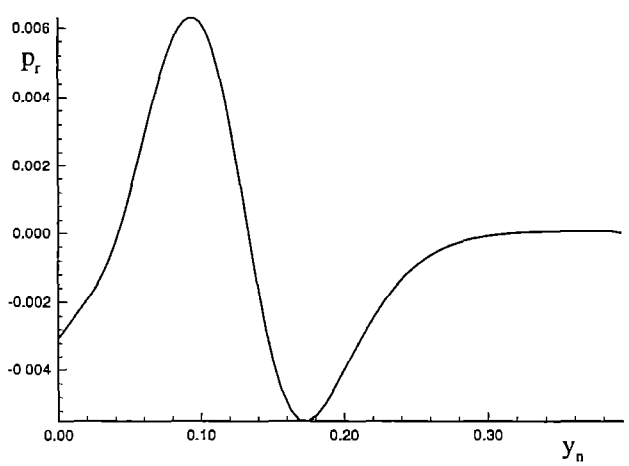

Figure 23: Eigenfunctions of the primary Görtler mode in inlet of zone7 at $G = 6.71$, $M = 7.89$, $Re = 4.23 \times 10^5$, and $\beta = 0.1$. Growthrate (σ_i) is 1.014.

Figure 24: Eigenfunctions of the second Görtler mode in inlet of zone7 at $G = 6.71$, $M = 7.89$, $Re = 4.23 \times 10^5$, and $\beta = 0.1$.Growthrate (σ_i) is 0.519.

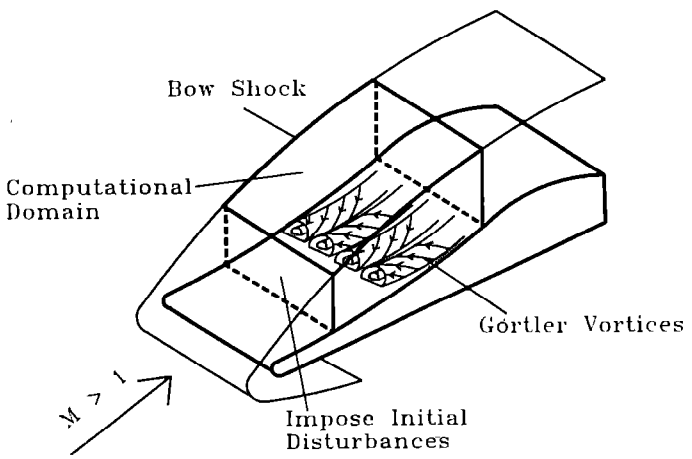

Figure 25: A schematic of the concave body(engine inlet) on which shock and Görtler vortices exist. Computational domain is shown in the figure

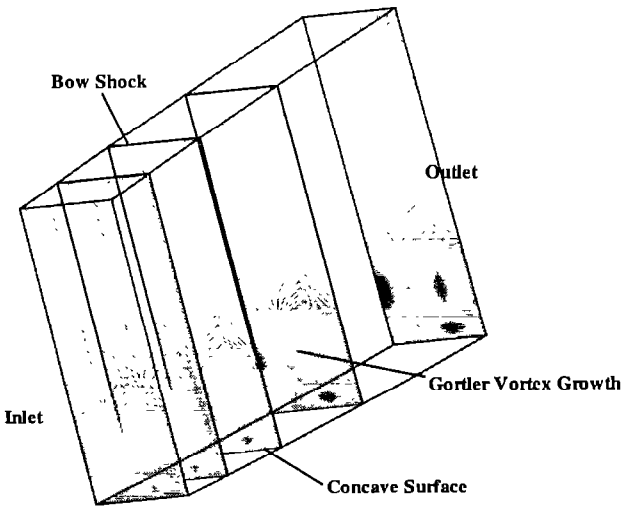

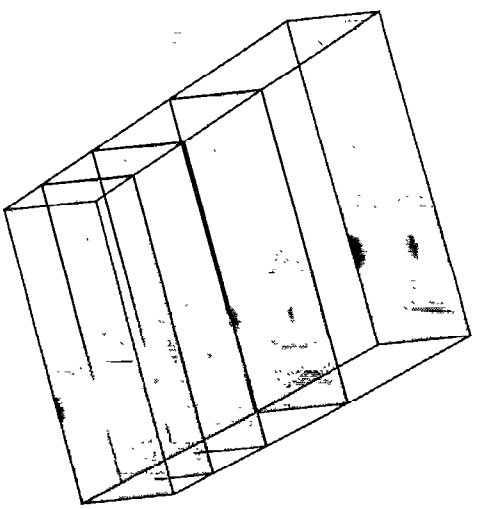

Figure 26: Temperature distribution of the primary(up) and second(bottom) Görtler modes along the streamwise direction at $G = 6.71$, $M = 7.89$, $Re = 4.23 \times 10^5$, and $\beta = 0.1$.

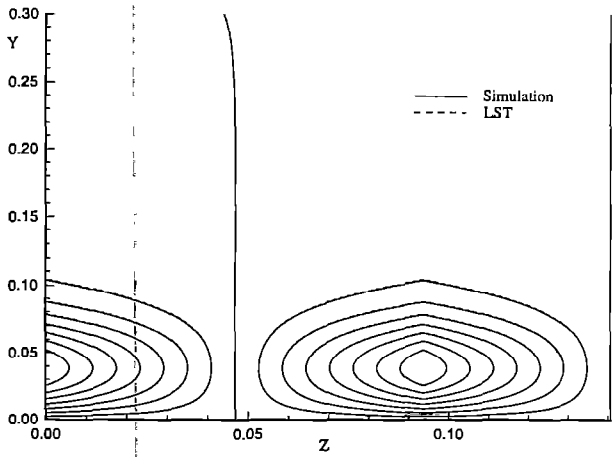

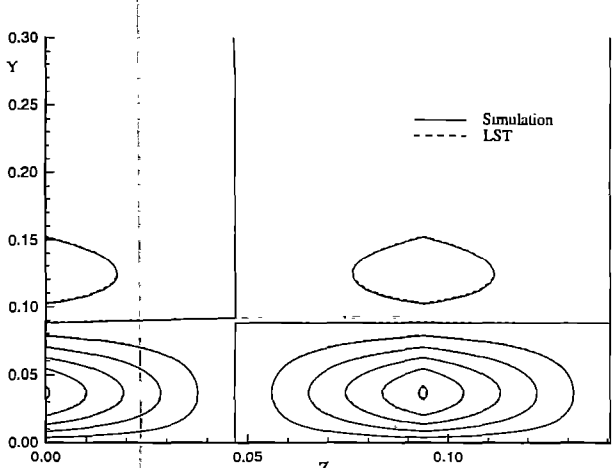

Figure 27: Velocity contours of the primary(up) and second(bottom) Görtler modes at I=100 of zone7 at $G = 6.71$, $M = 7.89$, $Re = 4.23 \times 10^5$, and $\beta = 0.1$. Results are compared with LST results.

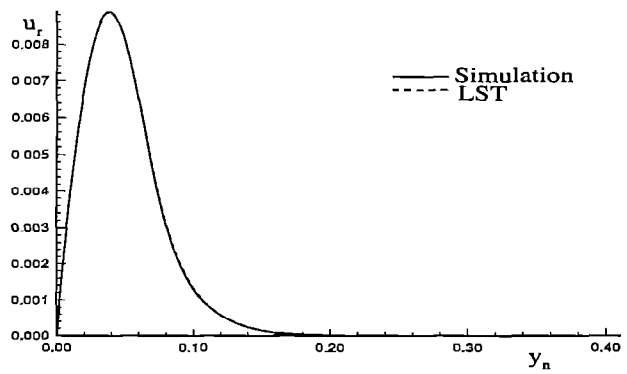

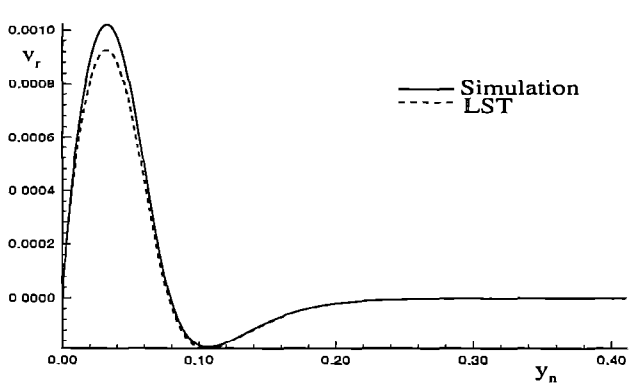

Figure 28: Distributions of u_r (up) and v_r (bottom) at I=100 of zone7 at $G = 6.71$, $M = 7.89$, $Re = 4.23 \times 10^5$, and $\beta = 0.1$. Results are compared with LST results

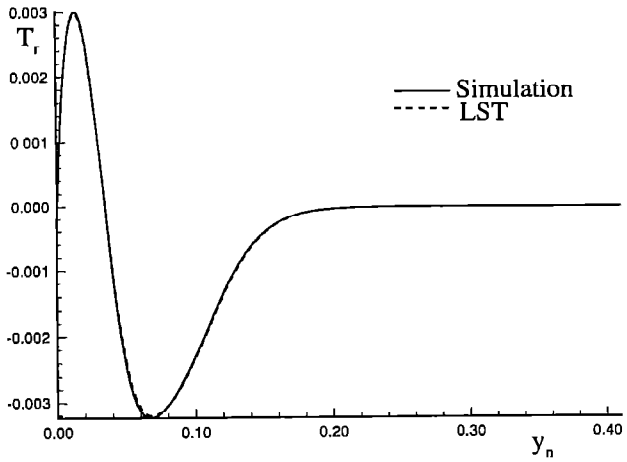

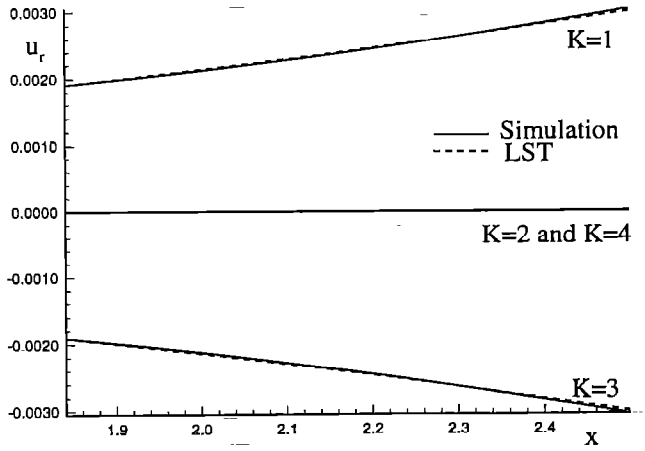

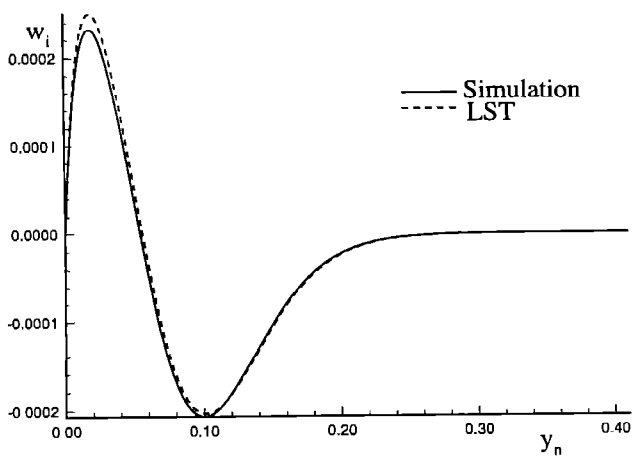

Figure 29: Distributions of T_r (up) and w_i (bottom) at I=100 of zone7 at $G = 6.71$, $M = 7.89$, $Re = 4.23 \times 10^5$, and $\beta = 0.1$. Results are compared with LST results

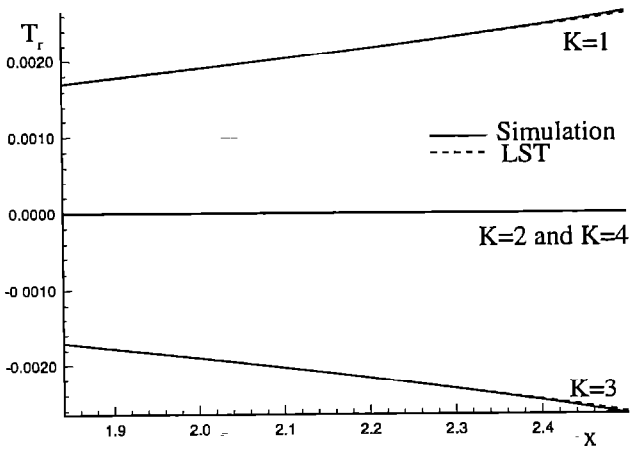

Figure 30: Distributions of u_r (up) and T_r (bottom) along streamwise direction at J=20 of zone7 at $G = 6.71$, $M = 7.89$, $Re = 4.23 \times 10^5$, and $\beta = 0.1$. Results are compared with LST results. It is shown that disturbances are growing along streamwise direction

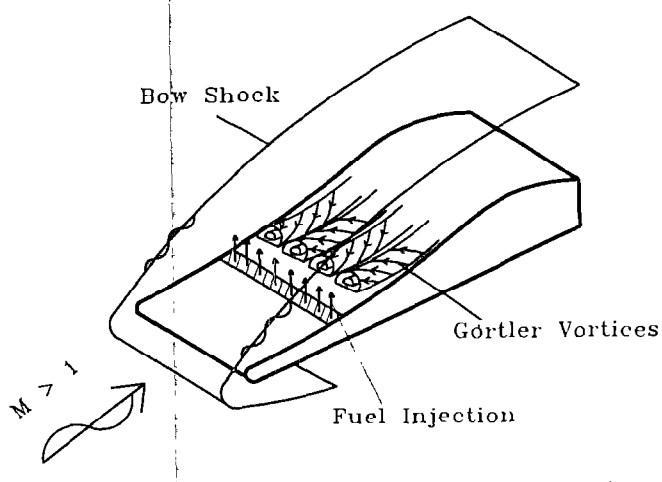

Figure 31: A schematic of the concave body(engine inlet) on which shock and Görtler vortices exist. Fuel injection is placed in front of the vortices.

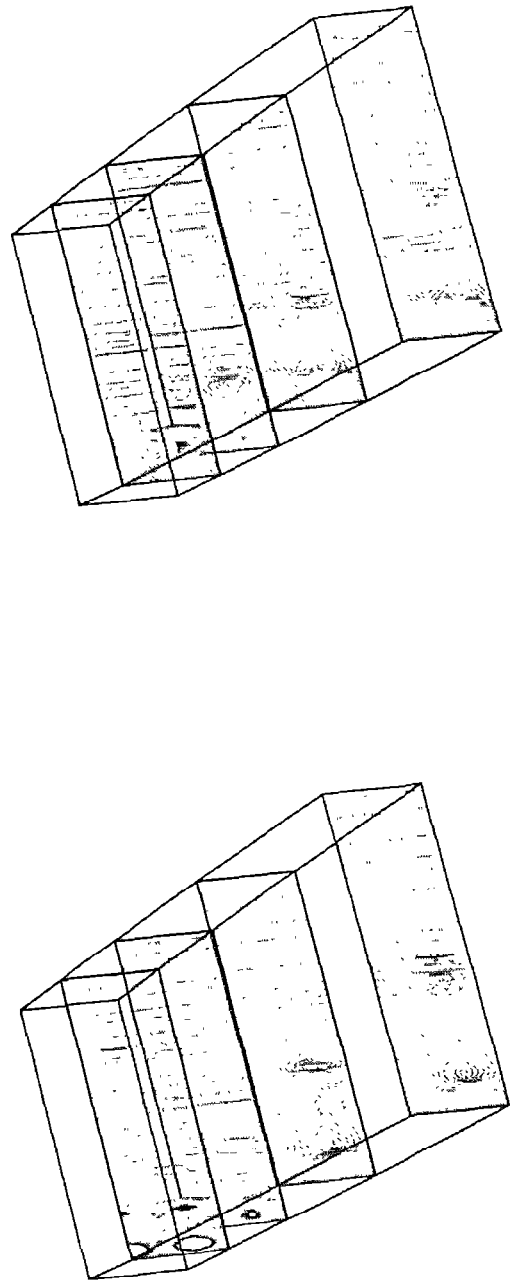

Figure 32: Distributions of velocity (u_r) and temperature (T_r) along the streamwise direction in zone 6 whose inlet contains blowing and section.

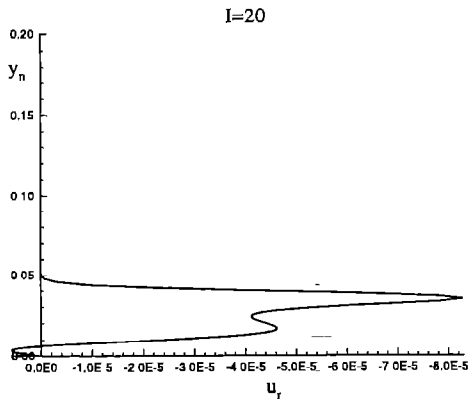

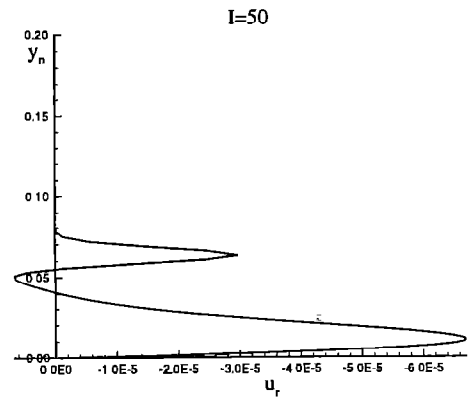

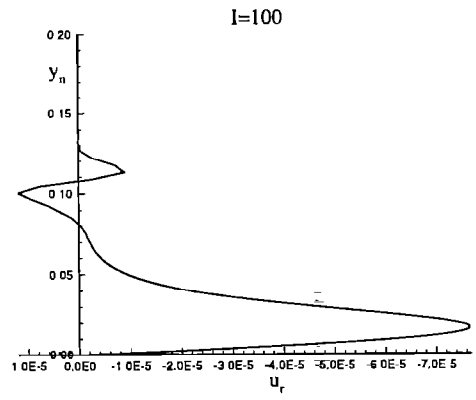

Figure 33: Velocity (u_r) profiles at three different locations. They show that there are two different disturbances, and top one is transitional disturbances and decays out.

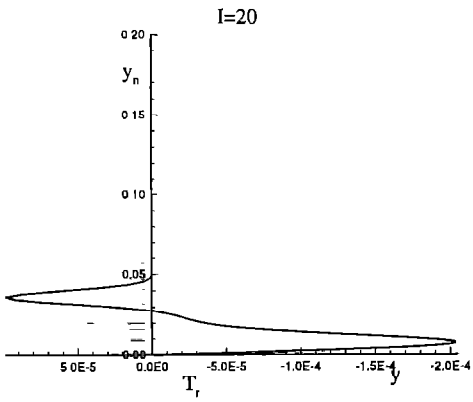

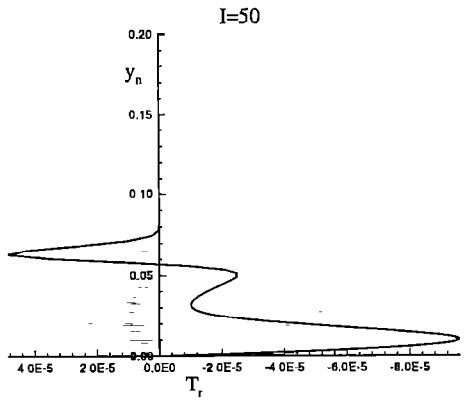

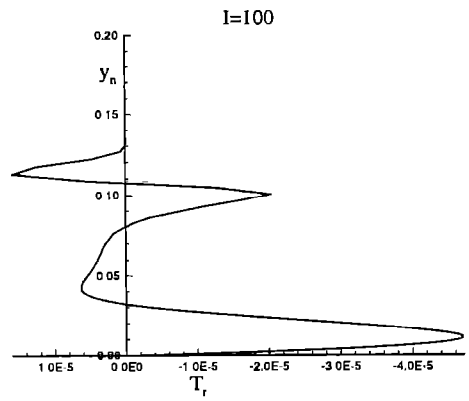

Figure 34: Temperature (T_r) profiles at three different locations.